

Figure 6.8: The temporal evolution of the average chemical content of the system, plotted for various values of permeability and porosity: (a)  $K = 10^{-14} \text{ m}^2$  and  $\phi = 0.1$ , (b)  $K = 10^{-13} \text{ m}^2$  and  $\phi = 0.1$ , (c)  $K = 10^{-14} \text{ m}^2$  and  $\phi = 0.01$ , and (d)  $K = 10^{-13} \text{ m}^2$  and  $\phi = 0.01$ . The values denote the excess salinity of the brine layer as compared to seawater.

gical conditions of the rocks, depletion by the dynamical mechanisms occurs on a shorter time scale than depletion across a purely diffusive/dispersive interface.

Especially the upward migration process gives rise to a short period of extremely high heat and mass transfer across the seafloor. However, this process cannot explain the megaplumes as observed in the seawater column, because these transient huge warm-water bodies are generally the first surface signal within a period of days after a magmatic event. This time interval is too short to generate a brine layer by phase separation and, subsequently, to flush out the brine by an upward migration of the interface. Since the magma supply at the base of the ridge crest is known to vary with time, however, the brine layer could have formed already during an earlier magmatic event such cancelling the time needed for producing the brine layer. Nonetheless, destabilization of an existing brine reservoir, by a next magmatic event can also be ruled out as to cause megaplumes: the high magmatic volatile content and salinity, associated with such a release, do not agree with the chemical signature generally observed in megaplumes [Baker, 1995; Palmer and Ernst, 1998].

From the experiments, we conclude that chronic venting of high-chlorinity fluids are indicative of the depletion of a static rather than convective brine layer. We have to be careful with this interpretation, though, as our model only considers the subcritical liquid phase: the

chronic high salinity vents may also be a surface signal of ongoing phase separation. In order to be able to distinguish between these two possibilities, simulations with multiphase flow in porous or fracture rocks are needed. Furthermore, in the simulations in which the interface is not very stable, the depletion of the brine will certainly be influenced by the transition from supercritical to subcritical conditions. With this in mind, strong temporal variations in the vent salinity measured at a single site are probably the result of ongoing phase separation in the underlying crust, rather than by a (subcritical) depletion of an already developed brine layer. Finally, the results described here may also be relevant in back-arc spreading regions and in continental geothermal systems where supercritical phase separation is observed [*Rona and Scott, 1993*].

# 7

## Chaotic thermohaline convection in low-porosity crust

### Abstract

Fluids circulate through the Earth's crust perhaps down to depths as great as five to fifteen kilometers, based on oxygen isotope systematics of exhumed metamorphic terrains, geothermal fields, mesozonal batholithic rocks and analysis of obducted ophiolites. Hydrothermal flows are driven by both thermal and chemical buoyancy; the former in response to the geothermal gradient and the latter due to differences in salinity that appear to be ubiquitous. Topographically driven flows generally become less important with increasing depth. Unlike heat, solute cannot diffuse through solid matrix. As a result, temperature perturbations advect more slowly than salinity fluctuations but diffuse more rapidly. Double-advection instabilities may play a significant role in solute and heat transport in the deep crust where porosities are low. We have studied the stability and dynamics of the flow as a function of porosity and thermal and chemical buoyancy for situations where mechanical dispersion of solute dominates over molecular diffusion in the fluid. In the numerical experiments, a porous medium is heated from below while solute provides a stabilizing influence. For typical geological parameters, the thermohaline flow appears intrinsically chaotic. We attribute the chaotic dynamical behavior of the flow to a dominance of advective and dispersive chemical transfer over the more moderate convective heat transfer, the latter actually driving the flow. Fast upward advective transport and lateral mixing of solute leads to formation of horizontal chemical barriers at depth. These gravitationally stable interfaces divide the domain in several layers of distinct composition and lead to significantly reduced heat flow for thousands of years. The unsteady behavior of thermochemical flow in low-porosity regions has implications for heat transport at mid-ocean ridges, for ore genesis, for metasomatism and metamorphic petrology, and the diagenetic history of sediments in subsiding basins.

### 7.1 Introduction

Virtually all of the oceanic crust to depths of 5 to 7 km, and also continental crust at depths greater than several kilometers, are characterized by a porosity which is small of order one volume percent or less [Huenges *et al.*, 1997; Fisher, 1998; Manning and Ingebritsen, 1999].

---

In revision by Schoofs, Spera and Hansen for *Earth Planet. Sci. Lett.*, 1999.

Aqueous fluids are present down to at least 9 km, based on deep borehole measurements [Kozlovsky, 1984; Liischen *et al.*, 1993; Möller *et al.*, 1997] and analysis of obducted ophiolites [e.g. Nehlig, 1994]. Further, it has been argued from oxygen isotope systematics of exhumed metamorphic terrains that fluids may penetrate down to 10 to 15 km [Nesbitt and Muehlenbachs, 1991]. The extensive collected works of Taylor and co-workers (see [Valley *et al.*, 1986] for a compilation) and others readily demonstrates the pervasive role played by fluids in mediating transport of heat and chemicals with the Earth's crust.

Large volumes of the Earth's crust although of low porosity may be fluid saturated. Provided sufficient permeability exists, these fluids advect within the deeper crust, driven by both thermal and chemical buoyancy; the former in response to the geothermal gradient, and the latter due to local variations in salinity, an almost inevitable consequence of complex geological processes. For example, very general and global mechanisms produce gradients in the salt concentrations within the fluid: meteoric water recharge from above (e.g. rain) while diagenetic, metamorphic and/or magmatic fluid sources lead to high concentrations of dissolved elements (up to saturation level) deeper within the crust [e.g. Hanor, 1994]. Advection of the saline fluids through the rocks has implications for many geological processes, such as heat transport, for ore genesis, for metasomatism and metamorphic petrology, and including the diagenetic history of sediments in subsiding basins [Bickle and McKenzie, 1987; Cathles, 1990; Furlong *et al.*, 1991; Newton *et al.*, 1998; Gerdes *et al.*, 1998; Tenthorey *et al.*, 1998; Aharonov *et al.*, 1998]. For an overview of these and other hydrogeological implications, the reader is referred to Person *et al.* [1996] and Ingebritsen and Sanford [1998].

When a fluid moves through a porous medium, heat and chemical elements can be transported by (1) diffusion through the interstitial liquid, (2) advection of the liquid and (3) molecular diffusion through the solid matrix. While diffusion of heat through the solid and liquid is of the same order, diffusion of chemical components through the liquid is much larger than through the solid. In addition to advective and diffusive transport of chemical elements, hydrodynamic mixing of the interstitial fluid at the pore scale also leads to chemical transfer. This type of mixing, also called mechanical dispersion, is due to obstructions and the fact that all pores may not be accessible to a fluid element after it has entered a particular flow path [Scheidegger, 1961]. Due to substantial heat diffusion through the solid rocks, mechanical dispersion of heat in the liquid is negligible under most geological circumstances [Kaviany, 1991; Nield and Bejan, 1992].

Heat and dissolved elements thus influence the interstitial fluid density in a different manner. Heat advects slower than chemical elements through the liquid by the factor  $\phi$ , while diffusion of heat through the bulk porous medium is larger by the factor  $\phi^{-1}$  times the ratio between the thermal and chemical diffusivities [Phillips, 1991]. Since the porosities are quite low of order  $10^{-2} - 10^{-4}$  in the deeper crust, double-advective double-diffusive instabilities may play a large role in the transport of solute and heat.

In this chapter, the stability and dynamics of the flow as a function of  $\phi$  and thermal and chemical buoyancy are investigated, for situations where dispersion of solute dominates over molecular diffusion in the fluid. In our numerical experiments, a low-porosity medium of aspect ratio one is heated from below, while solute provides a stabilizing influence. Figure 7.1a displays the configuration of the model together with two sets of boundary conditions. The first set consists of four impermeable boundaries (see Figure 7.1a). The dimensionless temperature and chemical concentration at the bottom boundary are equal to 1, while at the top both quantities are fixed to zero. The vertical walls are insulators with respect to heat and solute transport. The second set of boundary conditions is similar to the first one, except that the top boundary is permeable and isobaric (see Figure 7.1b). Initially, the fluid is motionless and the pressure distribution is zero everywhere. The interior is cold and chemically depleted.

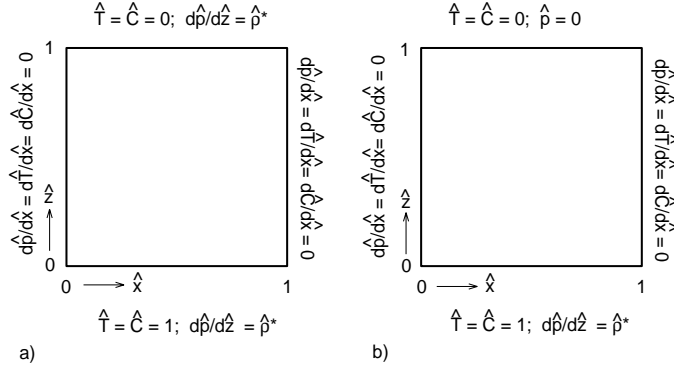


Figure 7.1: Geometrical setup and two sets of boundary conditions of the experiments in the porous medium, which is heated and salted from below: (a) closed, impermeable top and (b) open, permeable, isobaric top.

Note that heat destabilizes the liquid, while the solute provides a stabilizing influence.

The outline of this chapter is as follows. In section 7.2, the stability and dynamics of thermohaline convection in low-porosity media are described. After a few examples of the possible evolutionary states of the flow, we discuss the general picture of the fluid dynamical behavior as a function of the thermal and chemical buoyancy and porosity. The sensitivity of the convective flow to the boundary and initial conditions are discussed. A sensitivity study of the flow dynamics is also performed with respect to the anisotropic and dispersive character of the rocks. We conclude by summarizing the results and discussing the geological implications of this work.

## 7.2 Dynamics of low-porosity thermohaline convection

In this section, the stability and dynamics of thermohaline convection in low-porosity media are investigated for the case in which the porous medium is heated from below, while chemical concentration provides a stabilizing influence. We investigate the case in which mechanical dispersion of the solute dominates over molecular diffusion of the solute within the fluid. First, the results of a few numerical experiments are presented to give an overview of the possible evolutionary states (section 7.2.1). Next, the evolutionary states of the first set of experiments are discussed for a variety of porosities. The sensitivity of the fluid dynamical behavior to the boundary conditions (section 7.2.3) and the anisotropic permeability and dispersive character of the rock (section 7.2.4) is discussed. The spatial numerical resolution used is  $64 \times 64$  grid cells, based on extensive testing with different discretizations. The grid cells are concentrated in vertical direction near the base and the top of the domain in order to resolve the horizontal boundary layers.

### 7.2.1 Flow dynamics and transport properties: a few examples

In a first set of experiments, the thermal Rayleigh number  $Ra_T$ , the buoyancy ratio  $R_p$ , and the porosity  $\phi$  of the medium are varied systematically. All sides of the system are impermeable (see Figure 7.1a). Furthermore, permeability and porosity are isotropic and homogeneous throughout the domain. The transversal dispersivity is  $5 \times 10^{-5}$  times the vertical length

scale of the domain, while the dispersivity ratio is equal to  $a_r = 10$ . Initially, the motionless fluid is cold and chemically depleted, while the fluid is perturbed by giving the lower left grid point a temperature  $\hat{T} = 0.1$ .

Within the whole set of experiments, we have observed the system evolving to one of the following states: (1) static diffusive, (2) steady convective, (3) oscillatory convective, and (4) chaotic convective. The system of equations are integrated numerically until one of the stages can be clearly distinguished. At this point (1) the average velocity is smaller than  $10^{-4}$  and the heat flux through the domain is purely diffusive, (2) the average velocity is larger than  $10^{-4}$  and the difference between the surface heat flow and the globally averaged heat flow is smaller than  $10^{-4}$ , (3) at least five similar periods of the oscillation have been observed and, finally, (4) a statistically steady state has been reached.

Apart from the obvious static, diffusive solution, the observed evolutionary states of the flow are elucidated in three examples with  $Ra_T = 600$  and a porosity of  $\phi = 0.01$ . Dimensional parameters are used in the following, in order to give a better impression of the geological implications of the flow. The depth of the system is  $H = 4$  km, the temperature difference across the domain is  $\Delta T = 200^\circ\text{C}$ , and permeability is  $K = 5 \times 10^{-14} \text{ m}^2$ . The physical parameters of the system are given in Table 7.1, together with the thermodynamical fluid properties.

In Figure 7.2a-d the temperature and chemical distributions are depicted at four stages during the evolution of an experiment with a low chemical contrast of  $\Delta C = 2.5 \text{ wt\%}$  between top and bottom (corresponding with  $R_p = 0.25$ ). A dark (light) shading indicates a high (low) temperature or chemical concentration. Initially, a thermal boundary develops diffusively at the bottom of the domain, which quickly becomes unstable (Figure 7.2a,b). The thermally driven convective flow entrains salinity dispersively through the bottom of the domain into the interior (Figure 7.2b,c). Due to the low buoyancy of the chemicals, there is not much hindering force. The flow is therefore able to evolve rapidly towards a convective steady state, in this case consisting of four side-by-side slender cells (Figure 7.2d). The steady flow is characterized by three ascending plumes of hot, saline fluid, and two sinking colder and less saline currents in between. Note that solute advects 100 times faster than heat in this simulation. Thin thermal and even thinner chemical boundary layers are visible at the top and bottom of the domain. Since the solute transport is dominated by advection and/or dispersion throughout the domain, the interior is chemically well-mixed and nearly homogeneous at an average of  $C = 1.25 \text{ wt\%}$ .

Figure 7.3 shows the  $T$  and  $C$  distributions at four stages of an experiment with a slightly larger chemical contrast of  $\Delta C = 4 \text{ wt\%}$  between top and bottom. During the first  $10^5 \text{ yr}$  of the evolution, an irregular flow pattern is visible (Figure 7.3a), consisting of several irregular convection cells. The system frequently bifurcates to a flow pattern with another number of the cells. Furthermore, two different areas are observed within the whole domain, in which transport is mainly governed either by diffusion or advection. The diffusive areas, like the one

Parameter/notation	Value
Chemical contraction $\beta$	$1 \times 10^{-2} \text{ wt\%}^{-1}$
Dynamic viscosity $\mu$	$5 \times 10^{-4} \text{ Pa s}$
Reference density $\rho_0$	$1000 \text{ kg/m}^3$
Specific heat $C_w$	$4200 \text{ J/(kg K)}$
Thermal expansion $\alpha$	$5.0 \times 10^{-4} \text{ }^\circ\text{C}^{-1}$

Table 7.1: Thermodynamic fluid properties.

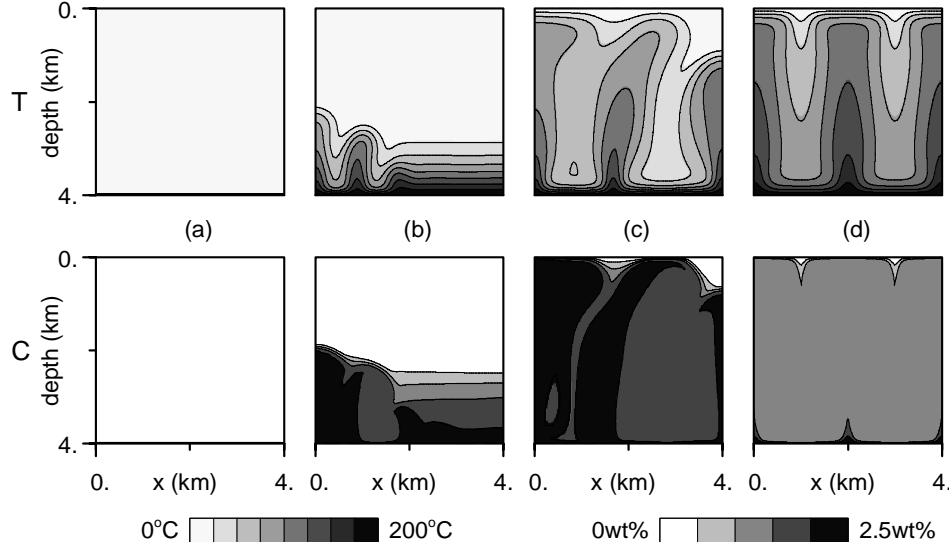


Figure 7.2: Snapshots of temperature  $T$  and compositional concentration  $C$  fields of a simulation with  $\Delta C = 2.5$  wt% and  $\phi = 0.01$  at (a)  $t = 0.0$  kyr, (b)  $t = 8.0$  kyr, (c)  $t = 40.0$  kyr, and (d)  $t = 200.0$  kyr. Light (dark) shading indicates low (high) temperature or enriched (depleted) compositional concentration. The corresponding dimensionless parameters are  $Ra_T = 600$ ,  $R_\rho = 0.25$ . The contour interval is  $25^\circ$  C and 0.5 wt%, respectively (see legends). Flow evolves towards steady state solution.

at the right-hand side of Figure 7.3a, are characterized by gradually increasing temperature and chemical concentration with depth, while the velocity is almost zero. In advective areas, on the other hand, vigorous convection of fluid has mixed the chemical concentration very well, while the temperature field is still smooth. As a result, these advective parts appear as chemically almost homogeneous spots within the chemical snapshots. Sharp chemical interfaces separate the diffusive and advective environments. Note that within the convective areas a significant amount of fluid recirculates. We will return to the issue of recirculation in section 7.2.3.

Suddenly, the convection evolves towards a fixed flow pattern of three side-by-side cells (Figure 7.3b). Due to the slightly unstable thermal boundary layers, variable amounts of chemical concentration enter or leave the domain dispersively through the top and bottom. As a result, the chemical content of the interior varies in an oscillatory fashion between  $\Delta C = 0.5$  and 3.5 wt%, with a period of 6 kyr (see Figures 7.3b-d).

Figure 7.4 displays the thermal and chemical distributions for an even larger chemical difference between the horizontal sides of the domain ( $\Delta C = 10$  wt%), at five different stages in the evolution. Figure 7.4a shows a hybrid pattern of advective and diffusive areas. In contrast to the previous experiment, the flow remains chaotic and reaches a statistically steady state. We attribute the chaotic behavior at larger chemical contrasts to the fact that the thermochemical system is dominated by advection, in this case, of principally one component: chemical concentration.

Another characteristic feature of the flow at low porosity is the spontaneous development of horizontal chemical barriers at depth. These gravitationally stable interfaces divide the domain into two or more separately convecting layers of a different chemical content. Rather than being an exception, the interface development is a common and prominent feature ob-

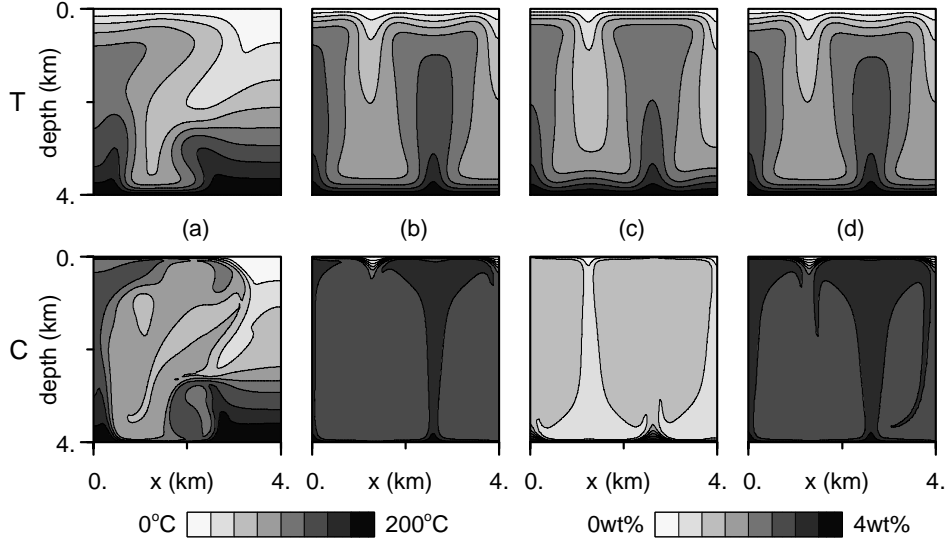


Figure 7.3: Temperature and solute snapshots of a flow which evolves towards an oscillatory state. The parameters are similar to those in Figure 3, except  $\Delta C = 4 \text{ wt\%}$  ( $R_p = 0.4$ ). The corresponding times are (a)  $t = 112.8 \text{ kyr}$ , (b)  $t = 513.6 \text{ kyr}$ , (c)  $t = 535.6 \text{ kyr}$ , and (d)  $t = 2736. \text{ kyr}$ . The contour interval are  $25^\circ\text{C}$  and  $0.5 \text{ wt\%}$  again.

served in low-porosity flow.

The formation and evolution of one of these interfaces is shown in Figures 7.4b up to 7.4e. In Figure 7.4a the interface is visible as the clustering of several horizontal isopleths at a depth of 2.4 km. Further convective mixing within the layers adjacent to the interface results in an increase of the chemical and thus density contrast across the interface up to a maximum of  $\Delta C = 9 \text{ wt\%}$  (Figure 7.4c).

When the convective vigor in the lower layer increases, fluid is entrained convectively from above the interface into the lower layer. Consequently, the density interface gradually migrates upward until it merges with the upper boundary layer such resulting in a single layered flow again (Figure 7.4c-e). Note that besides upward moving interfaces, we have also observed several interfaces migrating downward within the same experiment. For downward migration to occur, convection in the upper layer is more vigorous as compared to that in the lower layer. The migration of density interfaces which developed in an initially linearly stratified chemical concentration field is discussed in more detail in Chapters 4 and 5.

Besides explaining the various possible evolutionary states of the system, the three examples show an important effect of the chemically dissolved elements. Despite the stabilizing influence of salinity on the density profile, increasing the salinity difference between top and bottom results in a transition from steady to chaotic behavior. At the threshold value of the chemical to thermal buoyancy ratio, the convection is often characterized by an oscillatory flow pattern. We attribute the transition to an increasing influence of the transport of chemicals over the thermally driven flow field. The flow, although driven by a moderate thermal difference, appears intrinsically unsteady, due to the advectively and dispersively dominated transport of the solute.

In Figure 7.5 the temporal evolution of the heat and chemical fluxes through the top of the domain are shown for the three examples. Here, the heat flow through the surface of the

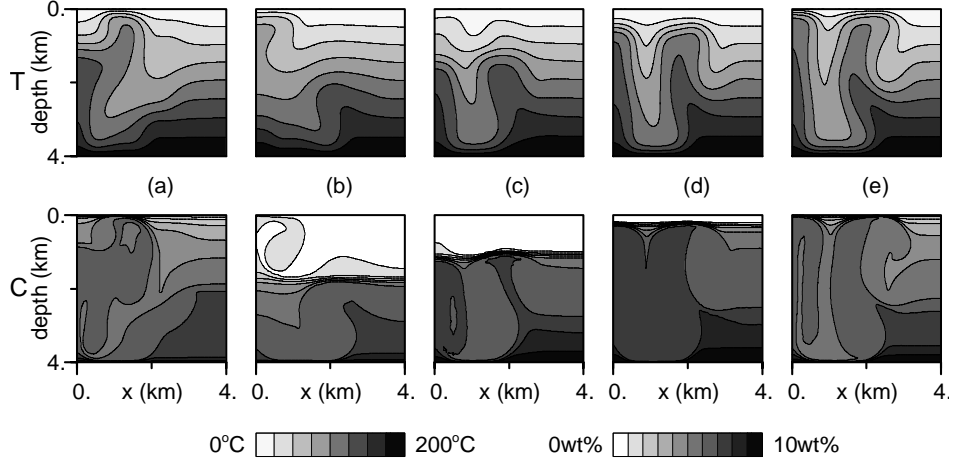


Figure 7.4: Temperature and salinity snapshots of a flow which remains chaotic. Parameters are similar to those in Figure 7.2 and 7.3, except  $\Delta C = 10 \text{ wt\%}$  ( $R_p = 1.0$ ). Snapshots b-e describe a cycle of the generation, migration and disappearance of a chemical interface at depth. The corresponding times are (a)  $t = 312.6 \text{ kyr}$ , (b)  $t = 320.2 \text{ kyr}$ , (c)  $t = 325.0 \text{ kyr}$ , (d)  $t = 327.2 \text{ kyr}$ , and (e)  $t = 329.4 \text{ kyr}$ . The contour interval is  $25^\circ\text{C}$  in the temperature plots and  $1 \text{ wt\%}$  in those of chemical concentration.

domain is defined as

$$q_T = -\overline{\lambda} \frac{\partial T}{\partial z}; \quad \text{at } d = 0\text{m}, \quad (7.1)$$

where  $d$  denotes the depth,  $\lambda (= 2.5 \text{ W/m}^\circ\text{C})$  the thermal conductivity, and the overbar implies a horizontal average. The chemical surface flux is defined as

$$q_C = -\overline{(\mathbf{D}_h \nabla C)_z}; \quad \text{at } d = 0\text{m}. \quad (7.2)$$

For the experiment with the lowest chemical contrast, the system evolves quickly to a steady state (Figure 7.5a,d). For the intermediate chemical contrast ( $\Delta C = 4 \text{ wt\%}$ ), both heat and solute transport become oscillatory after an initial stage of chaotic flow behavior (Figure 7.5b,e). When  $\Delta C = 10 \text{ wt\%}$  (Figure 7.5c,f), finally, both surface fluxes remain unsteady up to the end of simulation. Furthermore, the time-average of the chaotic heat flux is reduced as compared to the fluxes at a lower chemical contrast, because a part of the internal energy which enters the domain through the bottom is used to transport the dense chemical elements upwards. The smallest observed periods of the chemical flux are of the order of a few decades. These fluctuations are due to the variations in the chemical content of the advected fluid which reach the top of the domain. The highest frequency fluctuations are not present in the heat flux curves, because heat diffuses faster and advects at a slower rate as compared to solute. The periods between the large amplitude fluctuations correspond with the time needed for the formation and disappearance of the chemical interfaces. These time periods are therefore related directly to the migration speed of the interfaces.

The difference between the convective dynamics in the low, intermediate and high chemical concentration cases is further illustrated in the kinetic energy  $KE$  phase plots and power spectra shown in Figure 7.6. Here the spatially-averaged kinetic energy per unit mass of fluid

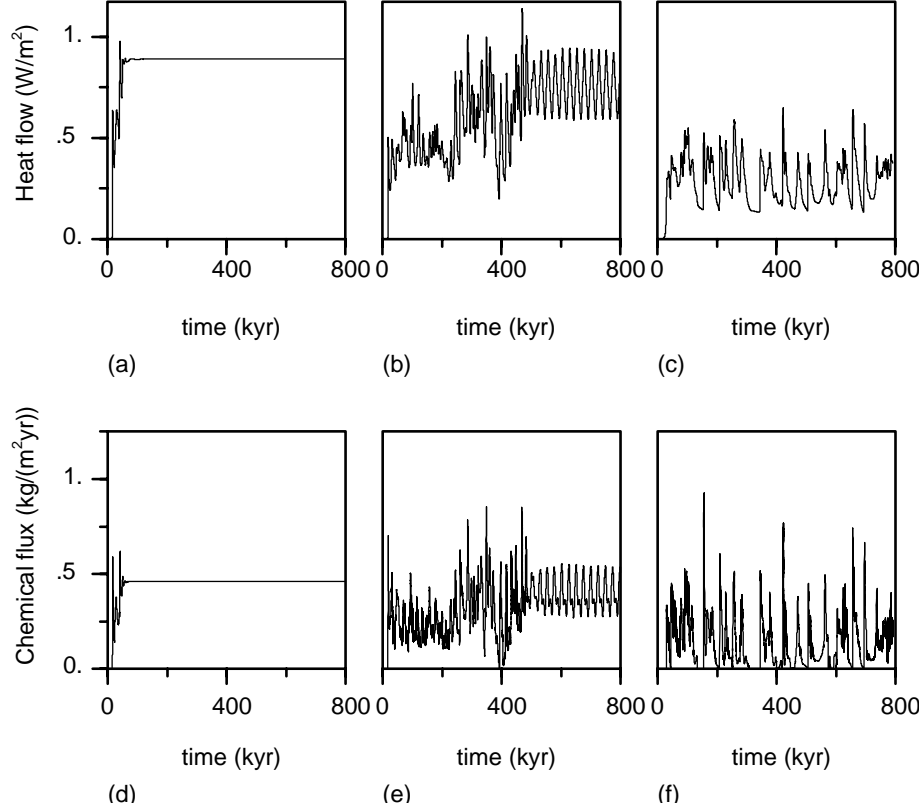


Figure 7.5: Temporal evolution of the (a-c) heat and (d-f) solute fluxes through the surface of the domain, for the experiments depicted in Figures 3, 4 and 5, respectively

$KE$ , which is a convenient measure of the vigor of the flow, is defined as

$$KE = \frac{1}{2} \langle q_x^2 + q_z^2 \rangle, \quad (7.3)$$

where the brackets denote the global average.

Figure 7.6a shows the  $KE$  phase plot for  $\Delta C = 2.5$  wt%. Here, the  $KE - \partial KE / \partial t$  trajectory spirals into a stable fixed point. Next, Figure 7.6b shows the  $KE$  phase plot for the second case, with  $\Delta C = 4$  wt%. The  $KE - \partial KE / \partial t$  trajectory follows an irregular orbit in a broader region of phase space, until it becomes a limit cycle (see the inset at the right top of the figure for a close-up view of the limit cycle). Note the different scales at the vertical axes. Furthermore, the average kinetic energy has decreased considerably, as compared to that for  $\Delta C = 2.5$  wt% at steady state. Finally, Figure 7.6c displays the  $KE$  phase plot for  $\Delta C = 10$  wt%. The  $KE - \partial KE / \partial t$  trajectory follows an irregular orbit in an even wider loosely defined region and never reaches a fixed point or limit cycle.

Figures 7.6d-f show the positive part of the power spectra for the three experiments at the time when the steady, oscillatory or statistically steady states have been reached. For calculating the power spectra, the averages of the signals have been subtracted and a boxcar window has been used. Figure 7.6d gives the power spectrum of the kinetic energy for  $\Delta C =$

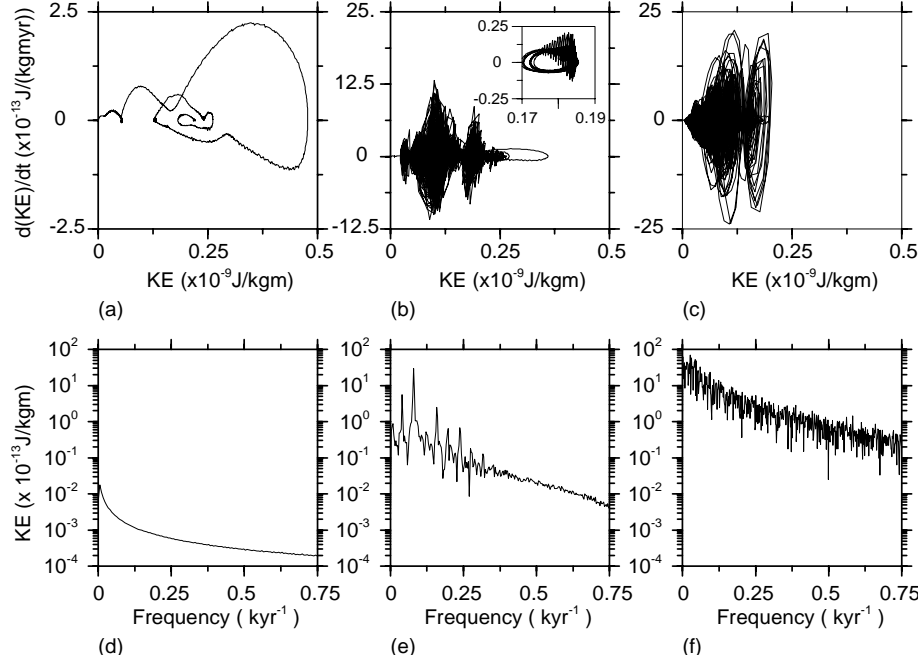


Figure 7.6: (a-c) The KE phase plots showing the trajectory in  $KE - \partial KE / \partial t$  space for the three experiments shown in Figures 3 - 5. (d-f) The accompanying positive parts of the power spectra of the kinetic energy, for periods in which the flow is in its final state of flow. Note that the average is subtracted from the signal.

2.5 wt%. No prevailing frequency is observed. The  $KE$  power spectrum for  $\Delta C = 4$  wt% is shown in Figure 7.6e. This power spectrum contains a single dominant frequency along with its harmonics. The peak with the lowest frequency corresponds with the period of the oscillation (being 25 kyr). Finally, the  $KE$  power spectrum for  $\Delta C = 10$  wt% is depicted in Figure 7.6f. In this case, the spectrum is characterized by broadband noise. The frequencies with maximal amplitudes are around  $2 \times 10^{-2} \text{ kyr}^{-1}$ . These frequencies correspond with the formation and migration of the chemical interfaces.

The petrological evolution of the host rock depends significantly on the temperature and salinity of the fluid at a fixed location. Therefore, we have plotted the temporal evolution of  $T$  and  $C$  at the center of the domain for the three simulations (see Figure 7.7). Obviously, the dynamical behavior of the flow is reflected directly in the thermal and chemical evolution of the fluid and thus the host rock. For the chaotic case, the passing of chemical interfaces results in salinity variations of up to  $\Delta C = 9$  wt% on time scales as short as a few decades. The flushing of the rocks with fluid of highly variable solute content may lead to alternating periods of over- and undersaturation of chemical within the fluid. Precipitation and dissolution of typical chemical elements could then easily produce the zonation, typically found in metamorphic rocks (e.g. banded sphalerite) [Bolton *et al.*, 1996].

Due to significant diffusion of heat, the thermal history of the rock is smoother as compared with the chemical one. Nevertheless, fluctuations up to half of the imposed temperature contrast between top and bottom are observed within periods of the order of a thousand years.

Results on the petrological history of a rock, as inferred from methods like oxygen isotope

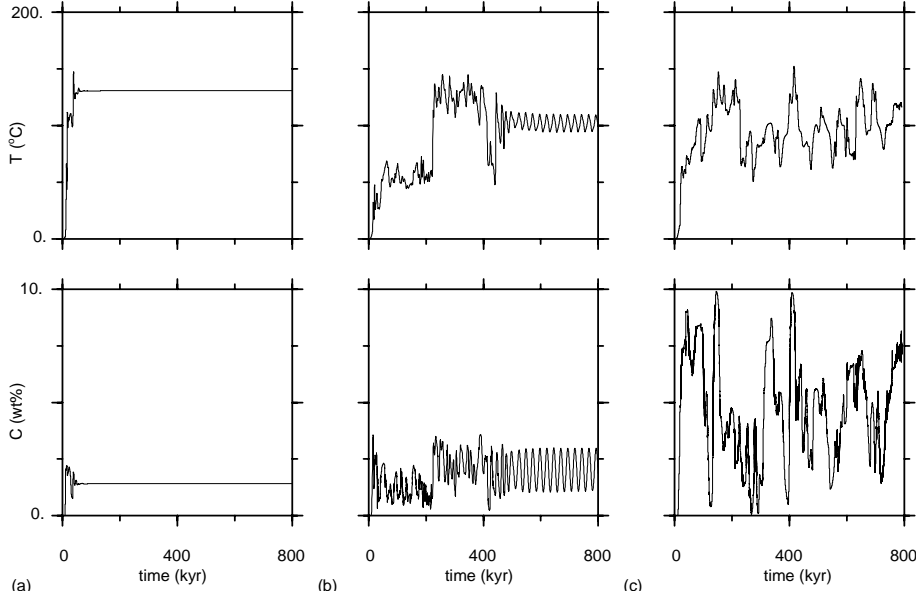


Figure 7.7: Temporal evolution of temperature (dotted curve) and salinity (solid) at the center of the domain ( $x = z = 2.0$  km). (a)  $\Delta C = 2.5$  wt%, (b)  $\Delta C = 4$  wt% (c)  $\Delta C = 10$  wt%.

analysis [Taylor, 1990] or fluid inclusion techniques [Roedder, 1984], are therefore very sensitive to the typical convective style of the flow. Salinities of distinct populations of preserved fluid inclusions within crystalline phases from many geothermal (including ore-forming) regions are very commonly found [Roedder, 1984; Saccoccia and Gillis, 1995]. The origin of these distinct populations may be related to the instabilities modeled in this study.

### 7.2.2 Flow regimes at various porosities

After discussing the possible evolutionary states of the system, we concentrate now on the distribution of these states within the  $Ra_T - R_p - \phi$  space which was sampled by our numerical experiments. Dimensionless parameters are used in order to give a more general picture. The flow space is plotted in Figure 7.8(a-c) for three porosities, as a function of  $Ra_T$  and  $R_p$ . The four different symbols denote the evolutionary states of the system and are explained in the figure caption.

Figure 7.8a shows the first case in which the medium has an hypothetical porosity of  $\phi = 1$ , which means actually that heat and solute advect with the same speed through the porous medium. At low buoyancy ratios,  $R_p \leq 0.25$ , the flow evolves to a steady or oscillatory convective solution when the thermal Rayleigh number is large enough to destabilize the fluid. Here, this critical Rayleigh number  $Ra_{T,\text{cr}}$  increases gradually with increasing buoyancy ratio. For increased buoyancy ratios, the commonality of chaotic flow is evident. Note that for pure thermally driven convection ( $R_p = 0$ ), the transition from oscillatory to chaotic convection occurs between  $Ra_T = 600$  and  $1000$ , that is, at a higher value than for thermochemical convection. Neither density interfaces or diffusive areas were observed in any of the experiments with  $\phi = 1$ , in contrast to flow at low porosity ( $\phi = 0.01$ ). Instead, convective currents directly connect the top and bottom of the system. The unsteady behavior of the flow

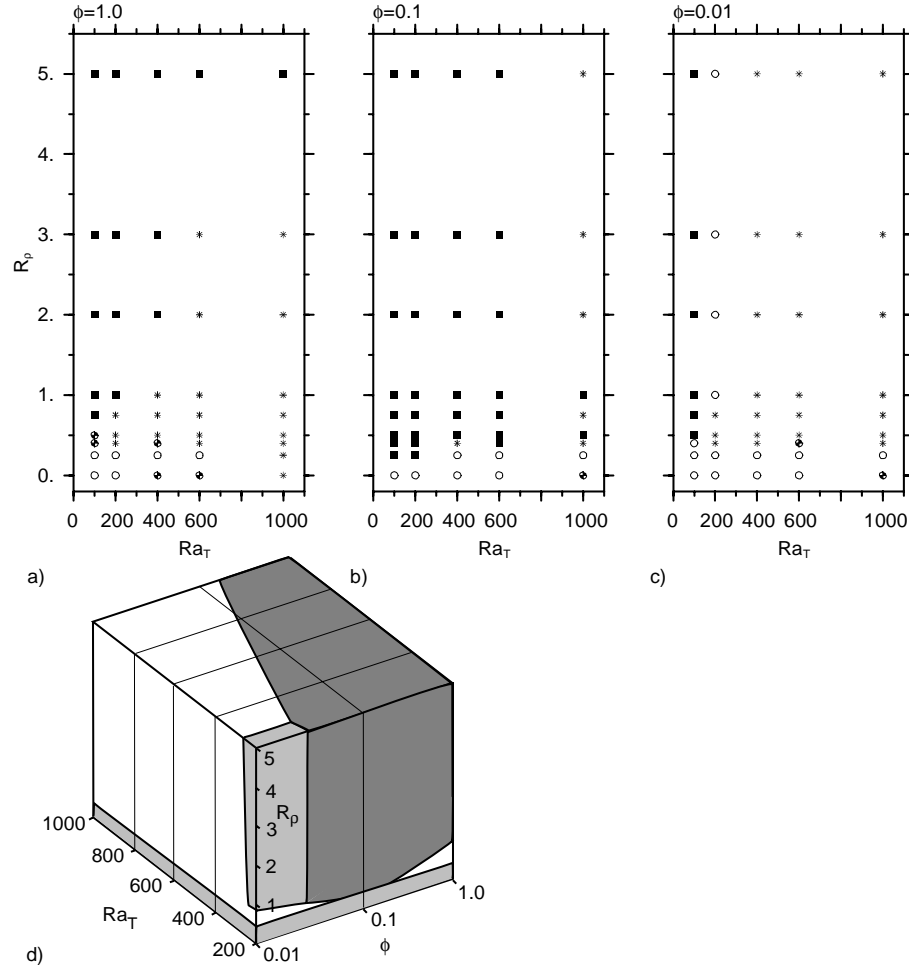


Figure 7.8: Evolutionary states of the system in  $Ra_T - R_p$  space, for (a) porosity equal to  $\phi = 1$ , (b)  $\phi = 0.1$ , and (c)  $\phi = 0.01$ . Here, (1) solid square indicates a static diffusive, (2) open circle a steady convective, (3) balloon an oscillatory convective, and (4) asterisk denotes a chaotic convective state. (d) Same evolutionary states, but now plotted on the surface of a cube with axes  $Ra_T$ ,  $\phi$  and  $R_p$ , as to show the appearance of the chaotic (white) regime at low porosity. The light-gray regimes include both steady and oscillatory convective states, while the flow evolves towards the static diffusive state in the dark-gray shaded regime.

is due to unstable boundary layers and cell bifurcations. Figure 7.8b shows the flow space for intermediate porosity ( $\phi = 0.1$ ). In most of the simulations, the flow evolves through a stage of irregular convective flow towards a static diffusive solution. During the chaotic stage in the evolution, the convective currents connect the top and bottom of the system again, while the formation of density interfaces is not observed. Diffusive areas do exist alongside convective patches within the flow domain, however, like in the low-porosity experiment shown in Figure

7.3. Despite the uniform heating and salting of the interior through the bottom, the difference in advection velocity of heat and solute apparently concentrates the vertical transfer of these quantities in laterally bounded areas.

At low porosity of the medium ( $\phi = 0.01$ ), finally, the convective dynamics are chaotic for nearly all simulations (see Figure 7.8c). The flow is characterized by diverse, complex flow patterns, consisting of first, the coexistence of diffusive and convective domains and, next, the formation, migration and disappearance of salinity interfaces. The dynamical behavior of the flow in low-porosity media is therefore fundamentally different from flow at higher porosity. The manifestation of this instability at typically low-porosity is visible in Figure 7.8d, where the evolutionary states are plotted on the surface of a cube with axes  $Ra_T$ ,  $\phi$  and  $R_p$ .

A few exceptions from the almost intrinsically unsteady character of the thermohaline driven flow at low porosity are observed. Apart from the obvious static diffusive solution which is obtained when the thermal buoyancy is not large enough to even drive convection without the presence of solute, the flow evolves to a steady or oscillatory state when  $R_p \leq 0.4$ , similar to flow at the higher porosities. Furthermore, in the regime of low thermal Rayleigh numbers ( $Ra_T = 200$ ) and large buoyancy ratios, a steady state solution is obtained consisting of a few side-by-side slender cells. The chemical horizontal boundary layers are embedded in the thermal ones completely, due to low chemical dispersion as compared with thermal diffusion. Since the chemical content is 'frozen' at the moment that the flow gets into the fixed pattern, the spatially averaged chemical concentration at steady state is different for each experiment.

From these experiments, we conclude that thermohaline convection is almost intrinsically chaotic at low porosity  $\phi = 0.01$ . We attribute this instability to a dominance of chemical transfer over the moderate heat transfer, which actually drives the flow. Since advection and dispersion of chemicals dominate significantly over molecular diffusion, the flow field appears unsteady.

The flow is characterized by the coexistence of advective and diffusive areas. Moreover, fast upward advective transport and lateral mixing of solute leads to the spontaneous generation of horizontal chemical barriers at depth. Since the chemical difference across the interface results in a stable density interface, separately convecting and chemically distinct layers develop on top of each other. These layers either grow or decline by the processes of advective and dispersive entrainment across the density interface(s). The period of time involved with the formation and disappearance of these interfaces determines the period between the major fluctuations of the flow. This convective style is fundamentally different from flow at intermediate and high porosities, which often evolve towards the static diffusive state.

Since the transition to chaos in three-dimensional experiments of pure thermally driven convection occurs at a lower thermal Rayleigh number as compared to two-dimensional experiments [Schubert and Straus, 1979], we expect that the observed intrinsical unsteadiness of low-porosity thermohaline convection is also present in a three-dimensional setting.

### 7.2.3 Fluid fluxes, recirculation and fluid-rock ratios

The gain, loss and/or exchange of chemical constituents of the solid rock via the fluid phase depends on the typical chemical reaction or dissolution rates involved as well as on the bulk flux and composition of the fluid. The efficiency of hydrothermal alteration of the rocks is therefore related to the absolute fluid flux (i.e. the total amount of fluid which passes a unit surface), temperature and, further, on the amount of recirculation. These quantities can be calculated by considering the volume flux of fluid across a horizontal plane as function of

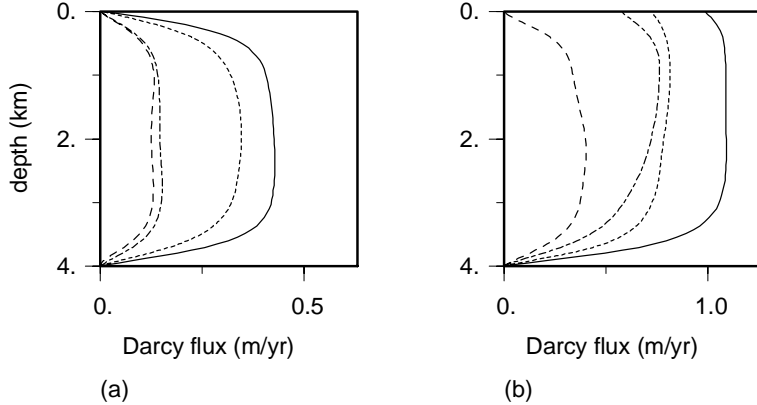


Figure 7.9: (a) Horizontally averaged vertical volume fluxes for various buoyancy ratios  $R_p$  plotted as a function of depth, for the case with an impermeable top boundary. The solid curve corresponds with  $R_p = 0.25$ , the dotted one with  $R_p = 0.5$ , the dash-dotted with  $R_p = 1$ , and the dashed curve with  $R_p = 2$ . Other parameters are  $Ra_T = 600$  and  $\phi = 0.01$ . (b) Similar as (a), except that the top boundary is permeable and isobaric.

depth. Geochemists and petrologists often use the concept of fluid-rock ratio to gauge the pervasiveness of fluid-driven metasomatism. This ratio is defined as the amount of fluid mass which passes a unit mass of rock.

It is apparent from the previous experiments that both porosity and the salinity contrast across the domain influence the pattern of the flow significantly. Besides the flow pattern, an increasing solute contrast may also affect the fluid flux through the rocks. In order to quantify the effect of salinity on the fluid flux, the horizontally averaged vertical volume fluxes are plotted as a function of depth in Figure 7.9a, for the set of experiments with  $Ra_T = 600$  and a porosity  $\phi = 0.01$ . The volume flux is time-integrated over a period of  $10^5$  yr to ensure a statistically average value. For low chemical contrasts between top and bottom ( $R_p < 1$ ), the upwelling and downwelling plumes are nearly vertical, while there is little exchange between these currents. This results in vertical fluid fluxes which are of the order of 30 to 40 cm/yr at mid-depth. Note that these fluxes give a water-rock ratio equal to 1 after only four years of pervasive flow, assuming an average density ratio of rock to water of 2.8.

For higher chemical contrasts ( $R_p \geq 1$ ), on the other hand, the flow is characterized by the generation and disappearance of horizontal density interfaces. During the existence of one or more interfaces, vertical fluid transport across the interface is negligible and all fluid recirculates within the convective layers above and below the interface(s). Consequently, the absolute vertical flux is reduced by a factor of three, as compared with pure thermally driven flow ( $R_p = 0$ ). Note that there is significant horizontal flow within the interior.

In these experiments, all fluid recirculates because the top boundary of the domain is impermeable. Rather than being closed, however, the surface is open and permeable in many geological situations. We have therefore performed a number of experiments in which a permeable, isobaric surface is considered (see Figure 7.1b). All other sides remain impermeable, and the boundary and initial conditions for temperature and chemical concentration are also similar as before.

Figure 7.9b shows the horizontally averaged vertical volume flux as a function of depth. For  $R_p < 0.5$ , the vertical fluid flux is nearly two times larger as compared to the case in which

the top boundary is closed. The surface fluid flux is, however, nearly equal to that at mid-depth because the fixed boundary conditions for  $T$  and  $C$  at the surface only slightly retard the vertical flow. For a buoyancy ratio of  $R_p = 2$ , finally, the horizontally averaged fluid flux is reduced by a factor of three as compared with that for pure thermally driven flow. More remarkably, despite the open boundary the surface flux has diminished almost completely.

### 7.2.4 Anisotropic Permeability and Mechanical Dispersion

Permeability is one of the most critical parameters governing the flow in geological systems. Although it is also one of the most difficult parameters to measure in the field (due to problems of heterogeneity and scale), the permeability field of both oceanic and continental crust is very likely anisotropic and heterogeneous [Brace, 1980, 1984; Huenges *et al.*, 1997; Fisher, 1998; Manning and Ingebritsen, 1999]. Flow through heterogeneous media is out of the scope of this chapter. For a detailed investigation of convection through heterogeneous media, the reader is referred to Chapter 8.

Several linear stability studies address the onset of thermal and thermohaline convection in anisotropic media [e.g. Castinel and Combarous, 1975]. Other studies focused on the amount of heat transport at slightly supercritical Rayleigh numbers [e.g. McKibbin, 1986]. Kvernold and Tyvand [1979] reported results on steady-state thermal convection in anisotropic media for anisotropy ratios ranging from 0.01 to 100 and for Rayleigh numbers up to approximately 10 times the critical Rayleigh number  $Ra_{T,cr}$  (where  $Ra_{T,cr}$  also varies with anisotropy). The influence of anisotropic permeability on the flow pattern for the oceanic crust was studied by Rosenberg *et al.* [1993]. The reader is referred to Storesletten [1998] for a review on convection in anisotropic media.

In this section, we are interested in the influence anisotropic permeability has on the dynamics of low-porosity thermochemical convection. Therefore, we have performed a set of experiments in a medium with  $\phi = 0.01$  in which the permeability ratios  $K_r = K_x/K_z = 0.1$  and 10 are considered. First a thermal Rayleigh number of  $Ra_T = 600$  is considered based on the vertical permeability, while the buoyancy ratio is varied between  $R_p = 0$  and 3. The other parameters are similar to those previously presented.

Figure 7.10a displays the evolutionary states of the experiments in a medium with  $K_r = 10$ . For all buoyancy ratios, the flow appears unsteady. The most prominent difference between the observed dynamical behavior as compared with experiments in an isotropic medium is that the aspect ratios of the convection cells are larger. Here, the aspect ratio is defined as the width of a convection cell divided by its length. For low buoyancy ratios ( $R_p \leq 0.25$ ), the flow pattern is characterized by a single convection cell. Oscillatory instabilities of the thermal boundary layers lead to a multi-periodic hydrological behavior. For larger buoyancy ratios, chemical interfaces develop again at depth and the flow appears very chaotic.

In Figure 7.10b the evolutionary states are shown as a function of  $R_p$ , for the case in which  $K_r = 0.1$ . For nearly all buoyancy ratios the flow evolves to a steady state in which the aspect ratios of the cells are small, as compared to flow in isotropic media. The chaotic character of the flow at  $R_p = 1$  is due to a nearly oscillatory bifurcation between a two-cellular flow pattern and that of a single slender convection cell and an adjacent diffusive area. The chemical reorganization involved with this bifurcation leads to an irregular behavior.

The differences between flow in isotropic and anisotropic media are primarily caused by the difference in the globally averaged permeability of these two media. In order to account for these linear effects of the anisotropy on the onset of convection and the vertical heat

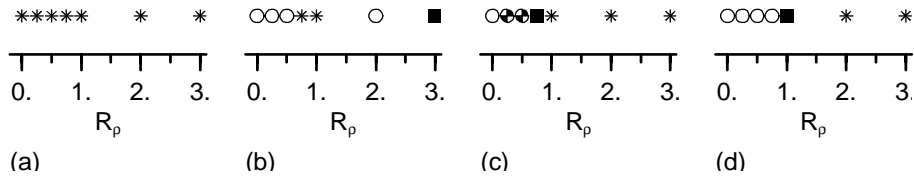


Figure 7.10: Sensitivity of behavior of the flow to the anisotropic permeability of the rock, as a function of the buoyancy ratio  $R_p$ . Parameters are  $Ra_T = 600$  and  $\phi = 0.01$ . The various flow states are explained in the caption of Figure 9. (a) Permeability ratio is equal to  $K_r = K_x/K_z = 10$ . (b)  $K_r = 0.1$ . (c) Similar permeability ratio as in (a),  $K_r = 10$ , but now for an effective thermal Rayleigh number of  $Ra_{T,\text{eff}} \approx 129.53$ . (d) Similar permeability ratio as in (b),  $K_r = 0.1$ , but now for an effective thermal Rayleigh number of  $Ra_{T,\text{eff}} \approx 1295.3$ .

transport in thermally driven flow, *Nield* [1997] proposed an effective thermal Rayleigh number  $Ra_{T,\text{eff}}$  rather than a Rayleigh number based on the vertical permeability. This effective Rayleigh number is defined as

$$Ra_{T,\text{eff}} = \frac{\alpha \rho g H \Delta T K_{SHR}}{\mu \kappa}, \quad \text{with} \quad K_{SHR} = 4 \left[ \frac{1}{K_x^{1/2}} + \frac{1}{K_z^{1/2}} \right]^{-2}. \quad (7.4)$$

Using this  $Ra_{T,\text{eff}}$ , both the onset of convection and the heat transport efficiency do not depend anymore on the degree of anisotropy. In order to investigate whether the transition from steady to chaotic thermochemical convection also scales with this effective  $Ra_{T,\text{eff}}$ , a set of experiments have been performed with the effective Rayleigh number as proposed by *Nield* [1997].

Figure 7.10c shows the case in which  $K_x$  is 10 times larger than  $K_z$ . In this case,  $Ra_{T,\text{eff}} \approx 129.53$ . For  $R_p \leq 0.5$ , the flow evolves to a steady or oscillatory convective state of two convection cells. The flow evolves through an initial chaotic stage towards the static diffusive solution when  $R_p = 0.75$ . For even larger buoyancy ratios, a single chaotic convection cell develops.

Figure 7.10d shows the evolutionary states for various  $R_p$ , for a permeability ratio  $K_r = 0.1$  ( $Ra_{T,\text{eff}} \approx 1295.3$ ). For low buoyancy ratios, the flow evolves to a steady pattern consisting of four to six side-by-side convection cells. The flow evolves through an initial chaotic stage towards the static diffusive solution when  $R_p = 1$ . For  $R_p \geq 2$ , finally, the flow appears unsteady and it consists of slender convection cells together with diffusive areas. Furthermore, due to the development of chemical interfaces intermittent stages of vertical layered convection are observed.

Comparison of the results of these experiments in anisotropic media with those obtained in isotropic ones (Figure 7.8c) indicates that, despite the use of a similar effective thermal Rayleigh number, we do not obtain a similar transition to chaos as compared with isotropic media. Irrespective of the anisotropic character of the permeability, however, the flow appears chaotic for almost all buoyancy ratios.

Mechanical dispersion of chemical concentration is another important factor which may influence the dynamics of the flow considerably. The amount of solute dispersion is related to the characteristic dispersion lengths of the porous medium: the longitudinal  $a_L$  and transversal  $a_T$  dispersivities. Like the degree of anisotropy in permeability, these two parameters also

vary considerably among hydrothermal systems. Furthermore, they are not well-constrained from field measurements for kilometer scale flow domains. Measured in-situ values of longitudinal dispersivity are of the order of 1 to 50 m, while the transversal component is up to an order lower [Gelhar, 1992; Schulze-Makuch and Cherkauer, 1997].

In the previous experiments, we have used the dimensionless dispersivities of  $\hat{a}_L = 5 \times 10^{-4}$  and  $\hat{a}_T = 5 \times 10^{-5}$ , which corresponds to the dimensional values of 2 and 0.2 meter for a system of 4 km depth, respectively. Though these values are in the range of measured values, they can also easily be larger by more than an order of magnitude. In order to study the sensitivity of the flow dynamics to chemical dispersion explicitly, we have increased the dispersivities to  $a_L = 40$  m and  $a_T = 10$  m. The permeability is assumed to be isotropic again.

In Figure 7.11a, the evolutionary states of the flow are plotted for the parameters  $Ra_T = 600$  and  $\phi = 0.01$ , as a function of  $R_p$ . The evolutionary states are almost similar to those with lower dispersion lengths, as can be seen by comparing Figure 7.11a with the results for  $Ra_T = 600$  in Figure 7.8c. Nevertheless, some differences between the flow in the two media are observed. From the results, we have the following indications for the dynamical consequences of mechanical dispersion. Locally, larger dispersion lengths of the medium lead to a more uniform chemical concentration. On the scale of the whole domain, on the contrary, the global averaged fluctuations of chemical concentration are large, as compared with the simulations in media with low dispersivities. This can be seen in Figure 7.11b in which the domain averaged chemical concentration is plotted against time, for the two dispersivities. Parameters are  $Ra_T = 600$ ,  $R_p = 1$  and  $\phi = 0.01$ .

### 7.3 Discussion and conclusions

Virtually all oceanic and the continental crust at depths greater than a few kilometers are characterized by a porosity which is quite small, of order 1 volume percent. However, fluids are commonly present and may remain so to depths of order 10 kilometers or more, as based on deep borehole measurements, oxygen isotope systematics of exhumed metamorphic terrains, and analysis of obducted ophiolites and mesozonal granitic rocks. These deep fluids may convect through the rocks, driven by both thermal and chemical buoyancy; the former in response to the geothermal gradient and the latter due to differences in salinity that appear to be ubiquitous.

We have investigated the stability and dynamics of thermochemically driven convective flow in these low-porosity environments ( $\phi = 0.01$ ), as a function of thermal and chemical buoyancy. Despite the stabilizing gravitational influence of the solute, increasing the salinity contrast between top and bottom of the domain (while keeping the temperature contrast constant) leads to a transition from steady to chaotic behavior of the convection. For typical geological parameters, the onset of chaotic behavior occurs when, at least for the two-dimensional flow studied here, the salinity contrast is approximately 5 wt% or more. Considering the large salinity gradients present within the crust, we conclude that advection of aqueous fluids appears intrinsically unsteady within vast volumes of the Earth's crust.

The chaotic dynamical behavior of the flow is due to the dominance of advective and dispersive chemical transfer over the more moderate convective heat transfer, the latter actually driving the flow. The flow pattern consists of distinct areas, in which heat and solute transport is governed either by advection or completely by diffusion. Furthermore, fast advective transport of solute enables the convective flow to spontaneously form horizontal chemical barriers at depth. These gravitationally stable interfaces divide the domain into two or more separately convecting layers of different composition. Advective and dispersive entrainment